Density and temperature reconstruction of a flame-induced distorted flow field based on background-oriented schlieren (BOS) technique*

Guang-Ming Guo(郭广明)† and Hong Liu(刘洪)

School of Aeronautics and Astronautics, Shanghai Jiao Tong University, Shanghai 200240, *China*

(Received 10 November 2016; revised manuscript received 6 February 2017; published online 20 April 2017)

An experimental system based on the background-oriented schlieren (BOS) technique is built to reconstruct the density and temperature distribution of a flame-induced distorted flow field which has a density gradient. The cross-correlation algorithm with sub-pixel accuracy is introduced and used to calculate the background-element displacement of a disturbed image and a fourth-order difference scheme is also developed to solve the Poisson equation. An experiment for a disturbed flow field caused by a burning candle is performed to validate the built BOS system and the results indicate that density and temperature distribution of the disturbed flow field can be reconstructed accurately. A notable conclusion is that in order to make the reconstructed results have a satisfactory accuracy, the inquiry step length should be less than the size of the interrogation window.

Keywords: background-oriented schlieren, density reconstruction, finite difference methods, distorted flow field

PACS: 47.10.–g, 47.11.Bc, 07.60.–j **DOI:** 10.1088/1674-1056/26/6/064701

1. Introduction

The density and temperature distribution of a flow field are the most important physical parameters because they essentially reflect the property of the fluid in the flow field. For example, the temperature distribution of a plume flow implies its infrared radiation feature, and the density fluctuation of a distorted flow field dominates the aero-optical effects of a beam passing through it.[1] The turbulent atmosphere has a great influence on the path of beam propagation due to the density gradient inside the atmosphere.[2] Thus, the development of diagnostic tools to obtain density and temperature information of a flow field has taken place in the area of aerodynamic research in the last few decades.[3,4] Generally speaking, the measurement techniques can be divided into two categories, that is, the intrusive and non-intrusive measurement. The intrusive measurement, such as thermocouples and pressure probes, can be used to measure the densities indirectly for constant pressure flows and isothermal flows.[5] However, they are essentially a point measurement technique. On the other hand, the non-intrusive measurement, such as the optical density measurement methods, has the advantage of capturing a complete two-dimensional (2D) density field. Most well-known optical density visualization techniques are schlieren photography, interferometry and shadowgraphy,[6] and all of these methods are based on line-of-sight integration of the variations in refraction index of the fluid within the measured volume. As a result, these techniques like schlieren and shadowgraph just provide qualitative information about the first and second derivative of density, respectively. Therefore, they are only suitable for the flow fields with relatively large jumps in density, such as shock waves. The major drawbacks of interferometry are the complexity in setting up such instrumentation and in fringe interpolation to determine the density fluctuations, which requires tremendous effort and care.[7] On the contrary, the instrumental requirement of the BOS technique is extremely modest. Usually, only one electronic camera, a background and a computer are needed. Other advantages of the BOS technique are its unlimited field of view and, consequently, its unlimited size of monitored objects.[8]

In recent years, the background-oriented schlieren (BOS) technique, first introduced by Meier and Dalziel,[9,10] has drawn attention as a novel measurement technique. The BOS technique is able to provide quantitative 2D density information,[7] and it also has a great potential for measuring a wide range of flows. Richard and Raffel[11] have successfully demonstrated the application of BOS to the large-scale density field measurement of helicopter-generated blade tip vortices. Unfortunately, neither theoretical nor numerical comparison with the measurements was given. Yamamoto *et al.*[12] used an ultra-high-speed imaging system based on the BOS technique to capture a laser-induced underwater shock wave. It indicated that the BOS technique is able to provide 2D density-gradient information about the flow field investigated and it only requires a simple setup. Venkatakrishnan[13] employed the BOS technique to obtain the mean density field of a complex under-expanded jet flow, and the presented density fields show that meaningful quantitative data can be extracted by using minimal hardware based on this technology. In addition,

*Project supported by the Key Program of the National Natural Science Foundation of China (Grant No. NSFC 91441205).

†Corresponding author. E-mail: guoming20071028@163.com

© 2017 Chinese Physical Society and IOP Publishing Ltd

he also used the BOS technique to obtain quantitative density distribution of supersonic flow around a cone–cylinder model in a wind tunnel. Mizukaki[14] used the BOS technique combined with a high-speed video camera as the recording device to achieve flow visualization, and it was also applied to shock-induced flow near the open end of a shock tube.

From the applications of the BOS technique that are reviewed above, it is seen that the density measurement by using the BOS has been investigated widely. However, to the best of our knowledge, the application of the BOS technique to temperature visualization has been demonstrated rarely. The reason is that the BOS is essentially a technique to reflect the refractive index distribution of a distorted flow field, which only contains density rather than temperature information. That is, the density distribution of the distorted flow field, rather than the temperature distribution, can be obtained based on the famous Gladstone–Dale expression (see Eq. (3)). However, if the relationship between density and temperature distribution is determined, the temperature distribution of the distorted flow field can also be obtained by the BOS. As a result, the reconstructed temperature distribution has the same precision as the density distribution obtained directly by BOS, which is a non-intrusive measurement technology and has high accuracy. In this paper, a fourth-order difference scheme is developed to solve the refractive index distribution of a flame-induced distorted flow field accurately, and both density and temperature distribution of the flame-induced distorted flow are reconstructed exactly based on iso-pressure hypothesis.

The rest of this paper is organized as follows. The BOS technique is introduced in Section 2, followed by a developed fourth-order difference scheme for density and temperature reconstruction in Section 3. Presented in Sections 4 and 5 are experimental arrangement and results, respectively. The last section (Section 6) is devoted to a simple summary for this study.

2. BOS technique

2.1. BOS theory

The principle of the BOS technique is based on the measurement of the deviation of a ray passing through a non-uniform object with a density gradient, which is similar to the conventional schlieren technique or specklegram technique. Actually, the BOS technique uses the local element displacement of a background image to detect the variation of refractive index of the non-uniform object due to its density gradient which is the first-order differential value of density. A schematic of the BOS technique is shown in Fig. 1.

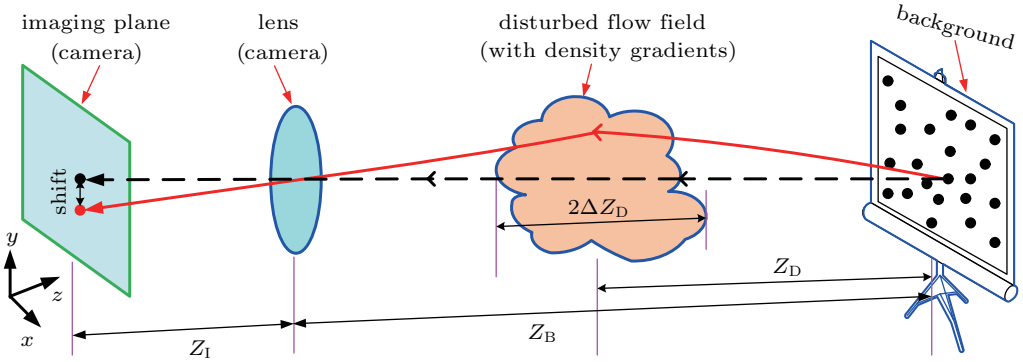


Fig. 1. (color online) Schematic diagram of the BOS technique. The black dash line represents a ray from a background point through the flow field without density gradient to the imaging plane, the red solid line denotes a ray from the same background point through the flow field with density gradient to the imaging plane.

As illustrated in Fig. 1, the path of a ray passing through the undisturbed flow field in which the density is approximately uniform is a straight line, whereas the trajectory of a ray from the same point traversing the disturbed flow field with density gradient is a curve, which results in a shifted image of the point in the imaging plane.[15] That is, the shift of a ray contains the information about the spatial gradient of the refractive index integrated along the light path through each point of the background pattern. For this reason, the shifts in the imaging plane can be related to the local density gradient of the investigated flow field, which is a flame-induced distorted flow in this study. For the BOS technique, the background-element displacements are obtained by comparing a reference image with a disturbed image via the cross-correlation algorithm.

Specifically, according to Venkatakrishnan and Meier,[7] the relationship between background-element displacement and refractive index gradient of the disturbed flow field is given by

$$\Delta x = \frac{Z_D \cdot Z_I}{Z_B} \cdot \frac{1}{n_0} \cdot \int_{Z_D-\Delta Z_D}^{Z_D+\Delta Z_D} \frac{\partial n}{\partial x} \mathrm{d}z, \tag{1a}$$

$$\Delta y = \frac{Z_D \cdot Z_I}{Z_B} \cdot \frac{1}{n_0} \cdot \int_{Z_D-\Delta Z_D}^{Z_D+\Delta Z_D} \frac{\partial n}{\partial y} \mathrm{d}z, \tag{1b}$$

where Δx and Δy are the background-element displacements in the horizontal direction (i.e., the x-axis direction) and vertical direction (i.e., the y-axis direction), respectively; Z_D is the distance from the background to the centre of a disturbed flow

field; Z_B is the distance from the background to the lens; Z_I is the distance from the lens to the imaging plane; ΔZ_D is half of the thickness of the disturbed flow field; n is the refractive index inside the disturbed flow field; n_0 is the refractive index of the undisturbed flow that is measured before the experiment; and z is the line-of-sight direction. Note that the background-element displacements obtained from Eqs. (1a) and (1b) essentially reflect integrated effects of refractive index gradients along the light path. For convenience, the constant coefficients in Eqs. (1a) and (1b) are denoted by

$$C = \frac{Z_D \cdot Z_I}{Z_B} \cdot \frac{1}{n_0}. \tag{2}$$

Using the law of Gladstone–Dale, the density can be directly related to the refractive index by

$$n = 1 + K_{GD} \cdot \rho, \tag{3a}$$

$$K_{GD} = 2.24 \times 10^{-4} \left(1 + \frac{7.52 \times 10^{-3}}{\lambda^2}\right), \tag{3b}$$

where ρ is the density of the flow field considered, λ is the wavelength of a beam, and K_{GD} is the Gladstone–Dale constant which has a value of approximately 2.27×10^{-4} m^3/kg in air for visible wavelengths of light.[1]

2.2. Background

Generally speaking, the equipment for the BOS technique consists of a camera for recording images, a computer for the image analysis, and a background. For the background, its pattern which is generated by a computer is also an important factor for the BOS technique. Usually, there are three types of backgrounds used for the BOS technique, and a small fragment of each type is shown in Fig. 2.

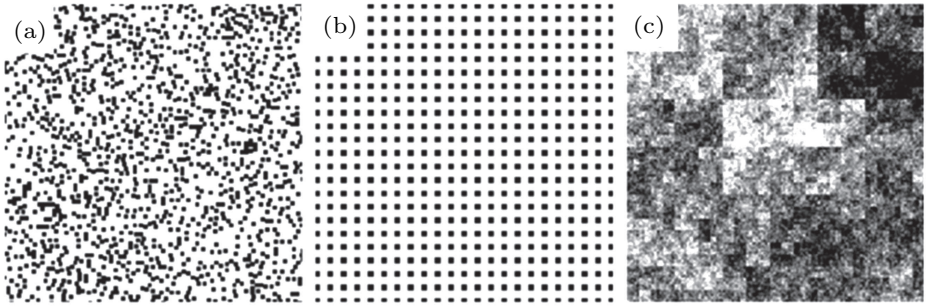


Fig. 2. Background patterns generated by a computer: (a) irregular, (b) regular, (c) wavelet-noise.

From Fig. 2, it is seen that the irregular background is composed of random dots, whereas the similar dots in the regular background are ranked regularly. Wavelet-noise background was first proposed in Ref. [16], and the details can be seen in it. For the BOS technique, an image recorded by a camera is just the grayscale image. Thus, the white dots and black background (or the black dots and white background) are considered preferentially as the background pattern due to their fine contrast ratio.

In this study, the cross-correlation algorithm is used to calculate the background-element displacement of the background in a distorted flow field. In addition, it is known that the calculated background-element displacement is the critical factor in reconstructing the density and temperature distribution of the distorted flow field (see Eq. (1a)), so the type of background should be chosen appropriately for the cross-correlation algorithm.

According to the analysis given by Vinnichenko *et al.*,[17] the regular backgrounds have certain disadvantages because they show similar behaviors for their periods. If the displacement of an interrogation window is larger than or equal to the pattern period, two identical correlation peaks emerge and interrogation fails. For the wavelet-noise pattern, it is much more vulnerable with respect to blur than the background with randomly distributed dots, and it is usually employed by combining with the optical flow algorithm.[18] Actually, the background with irregular dots is used widely in the BOS technology and it is especially suitable for the cross-correlation algorithm. What is more, it has an optimal performance if the dot image size is approximately 3 pixels, and for this background the reconstructed density and temperature distribution are able to achieve satisfactory accuracy if the step length is less than the size of the interrogation window (see Subsection 5.3). Therefore, the background with irregular dots is chosen as the experimental background of the BOS built in this study.

2.3. Cross-correlation algorithm

The background-element displacement in the horizontal and the vertical direction (i.e., Δx and Δy) between a reference image and a disturbed image is calculated via two identical interrogation windows in both images by using the cross-correlation algorithm originally developed for PIV,[19] the schematic of cross-correlation algorithm is shown in Fig. 3, where the coordinate of the central pixel of each interrogation window is denoted as the position of the corresponding inter-

rogation window, such as (x_0, y_0) for the interrogation window in the reference image and (x', y') for the interrogation window in the disturbed image. In addition, the u and v are marked as the integer pixel displacements in the horizontal (x) and vertical (y) direction, respectively. The size of the interrogation window for this study is a typical dimension of 32×32 pixels, and the area surrounded by the green rectangle is the search region.

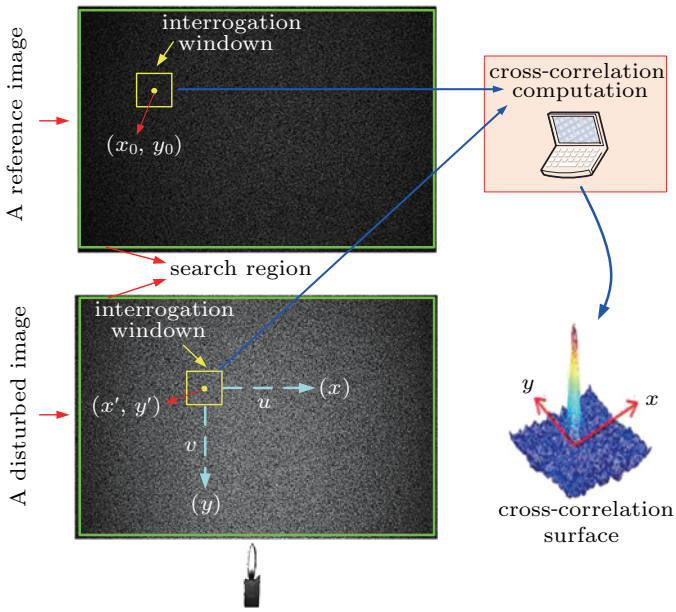


Fig. 3. (color online) Schematic diagram of the cross-correlation algorithm.

$$R(u,v) = \frac{\sum_u \sum_v f(x,y) \cdot g(x+u, y+v)}{\sqrt{\sum_u \sum_v f^2(x,y) \cdot g^2(x+u, y+v)}}. \tag{4}$$

The cross-correlation calculation is the core of the cross-correlation algorithm as given by Eq. (4), where the term $f(x,y)$ represents the grayscale distribution over the interrogation window in the reference image and the term $g(x+u, y+v)$ denotes that in the disturbed image. Note that the interrogation window in the disturbed image is shifted by only one pixel along the horizontal or the vertical direction for each cross-correlation calculation, whereas its corresponding interrogation window in the reference image is always stationary during these cross-correlation calculations.

The value of $R(u,v)$ varies between 0 and 1. For $R(u,v) = 0$, it is an indication of no relationship between the two interrogation windows in both reference and disturbed images; whereas for $R(u,v) = 1$, it means that the two interrogation windows are exactly the same. As a matter of fact, for the two matching interrogation windows, the value of $R(u,v)$ just approximately equals 1.0.

As mentioned above, the cross-correlation algorithm described above only produces pixel-level accuracy because the interrogation window is shifted by integer pixels for both horizontal and vertical directions in the disturbed image. To obtain the sub-pixel-level accuracy, one can either interpolate the cross-correlation surface to a higher resolution by using a 2D interpolation algorithm or fit a 2D analytical function to the cross-correlation surface around the peak.[20]

Actually, the cross-correlation surface around its peak usually approaches to a bell shape. Thus, in this paper, we use Gaussian fitting which has been tested successfully by empirical and theoretical researches to seek the more accurate peak position with sub-pixel-level. In the Gaussian fitting, the bell shape of the cross-correlation surface is assumed to fit a 2D Gaussian function,[21] and it is assumed that the two directions (i.e., x and y directions) are separable from and orthogonal to each other. For this reason, the sub-pixel-level peak location is calculated separately for the two directions by fitting a second-order polynomial to the direct neighbors of the point (x', y') as illustrated in Fig. 4, and the computational formulae for sub-pixel-level displacements in both directions are given by Eqs. (5a) and (5b).

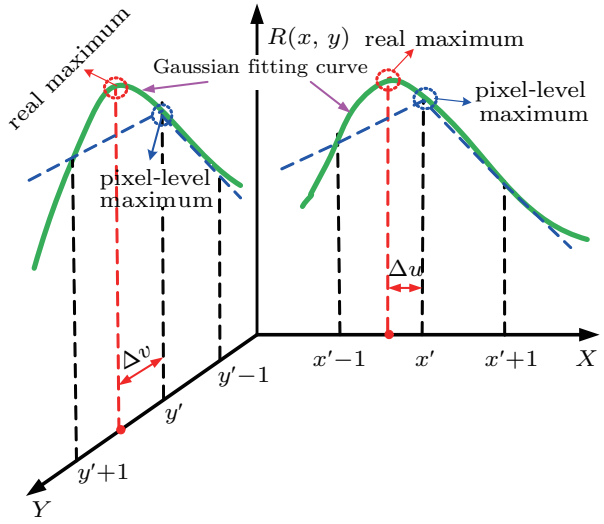


Fig. 4. (color online) Sketch of the exact peak location solved by Gaussian fitting.

$$\Delta u = \frac{\ln(R(x'-1,y')) - \ln(R(x'+1,y'))}{2\ln(R(x'+1,y')) - 4\ln(R(x',y')) + 2\ln(R(x'-1,y'))}, \tag{5a}$$

$$\Delta v = \frac{\ln(R(x',y'-1)) - \ln(R(x',y'+1))}{2\ln(R(x',y'+1)) - 4\ln(R(x',y')) + 2\ln(R(x',y'-1))}. \tag{5b}$$

Then, the displacement of the point (x_0, y_0) that has sub-pixel-level precision in both horizontal and vertical directions is calculated by

$$\Delta x = u + \Delta u, \quad \Delta y = v + \Delta v. \tag{6}$$

3. Density and temperature reconstruction

3.1. Poisson equation

As revealed in Eqs. (1a) and (1b), the background-element displacement is proportional to refraction index gradient in both horizontal and vertical directions. Actually, the Poisson equation which describes the refraction index distribution in a disturbed flow field can be derived from Eqs. (1a) and (1b) as follows:

$$\frac{\partial^2 n}{\partial x^2}+\frac{\partial^2 n}{\partial y^2}=C\cdot\left[\frac{\partial \Delta x}{\partial x}+\frac{\partial \Delta y}{\partial y}\right]. \tag{7}$$

If the background-element displacements (i.e., Δx and Δy) have been known, solving the Poisson equation (7) still requires boundary conditions. Generally, the boundary conditions are assumed to be free from disturbance, so the refraction index of the undisturbed flow field that is measured before experiment and the corresponding background-element displacements are used as the specific boundary conditions in this study.

3.2. High-precision difference scheme

There are many methods of solving the Poisson equation, and the well-known one is finite difference which has various iteration schemes. In this paper, a fourth-order difference scheme is developed to solve the Poisson equation. For a 2D computation plane, the discrete refraction index distribution around a point whose value is unknown can be shown in Fig. 5, where h is the interval of grids, the subscripts "0, 1, 2, ...," denote the position of each point. Thus, the n_0, for example, means the refractive index of point "0". It is found in Fig. 5 that the difference scheme requires nine points in calculation when it runs. The refractive index of the point located in the centre (i.e., n_0) is unknown and it is solved via its ambient eight points whose refractive indices can be known by assigning an initial value for each of them.

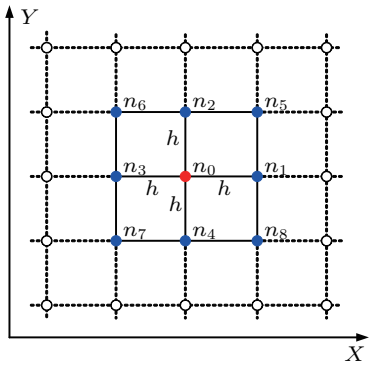


Fig. 5. (color online) Schematic diagram of the discrete refraction index distribution in a 2D plane.

Firstly, in order to deduce the fourth-order difference scheme, Taylor decomposition is applied to the eight external points. Taking the n_1 and n_5 for example, the decomposed results are given as follows:

$$\begin{aligned} n_1 &= n_0+h\cdot\frac{\partial n}{\partial x}+\frac{h^2}{2!}\cdot\frac{\partial^2 n}{\partial x^2}+\frac{h^3}{3!}\cdot\frac{\partial^3 n}{\partial x^3}+\frac{h^4}{4!}\cdot\frac{\partial^4 n}{\partial x^4}\\ &\quad+\frac{h^5}{5!}\cdot\frac{\partial^5 n}{\partial x^5}+\frac{h^6}{6!}\cdot\frac{\partial^6 n}{\partial x^6}+\frac{h^7}{7!}\cdot\frac{\partial^7 n}{\partial x^7}+O(h^8), \end{aligned} \tag{8a}$$

$$\begin{aligned} n_5 &= n_0+h\cdot\left[\frac{\partial n}{\partial x}+\frac{\partial n}{\partial y}\right]+\frac{h^2}{2!}\cdot\left[\frac{\partial^2 n}{\partial x^2}+2\frac{\partial^2 n}{\partial y\partial x}+\frac{\partial^2 n}{\partial y^2}\right]\\ &\quad+\frac{h^3}{3!}\cdot\left[\frac{\partial^3 n}{\partial x^3}+3\frac{\partial^3 n}{\partial x\partial y^2}+3\frac{\partial^3 n}{\partial y\partial x^2}+\frac{\partial^3 n}{\partial y^3}\right]\\ &\quad+\frac{h^4}{4!}\cdot\left[\frac{\partial^4 n}{\partial x^4}+4\frac{\partial^4 n}{\partial x^3\partial y}+6\frac{\partial^4 n}{\partial x^2\partial y^2}+4\frac{\partial^4 n}{\partial x\partial y^3}+\frac{\partial^4 n}{\partial y^4}\right]\\ &\quad+\frac{h^5}{5!}\cdot\left[\frac{\partial^5 n}{\partial x^5}+5\frac{\partial^5 n}{\partial x^4 y}+10\frac{\partial^5 n}{\partial x^3 y^2}\right.\\ &\quad\left.+10\frac{\partial^5 n}{\partial x^2 y^3}+5\frac{\partial^5 n}{\partial x\partial y^4}+\frac{\partial^5 n}{\partial y^5}\right]\\ &\quad+\frac{h^6}{6!}\cdot\left[\frac{\partial^6 n}{\partial x^6}+6\frac{\partial^6 n}{\partial x^5\partial y}+15\frac{\partial^6 n}{\partial x^4\partial y^2}+20\frac{\partial^6 n}{\partial x^3\partial y^3}\right.\\ &\quad\left.+15\frac{\partial^6 n}{\partial x^2\partial y^4}+6\frac{\partial^6 n}{\partial x\partial y^5}+\frac{\partial^6 n}{\partial y^6}\right]\\ &\quad+\frac{h^7}{7!}\cdot\left[\frac{\partial^7 n}{\partial x^7}+7\frac{\partial^7 n}{\partial x^6\partial y}+21\frac{\partial^7 n}{\partial x^5\partial y^2}+35\frac{\partial^7 n}{\partial x^4\partial y^3}\right.\\ &\quad\left.+35\frac{\partial^7 n}{\partial x^3\partial y^4}+21\frac{\partial^7 n}{\partial x^2\partial y^5}+7\frac{\partial^7 n}{\partial x\partial y^6}+\frac{\partial^7 n}{\partial y^7}\right]+O(h^8). \end{aligned} \tag{8b}$$

The rest, such as n_2, n_3, n_4, and n_6, n_7, n_8, can be obtained easily by utilizing the symmetry of these points. Then, we can obtain the following formulae:[22]

$$\begin{aligned} M &= n_1+n_2+n_3+n_4=4n_0+h^2\cdot\left[\frac{\partial^2 n}{\partial x^2}+\frac{\partial^2 n}{\partial y^2}\right]\\ &\quad+\frac{h^4}{12}\cdot\left[\frac{\partial^4 n}{\partial x^4}+\frac{\partial^4 n}{\partial y^4}\right]+\frac{h^6}{360}\cdot\left[\frac{\partial^6 n}{\partial x^6}+\frac{\partial^6 n}{\partial y^6}\right]+O(h^8), \end{aligned} \tag{9a}$$

$$\begin{aligned} N &= n_5+n_6+n_7+n_8=4n_0+2h^2\cdot\left[\frac{\partial^2 n}{\partial x^2}+\frac{\partial^2 n}{\partial y^2}\right]\\ &\quad+\frac{h^4}{6}\cdot\left[\frac{\partial^4 n}{\partial x^4}+\frac{\partial^4 n}{\partial y^4}\right]+h^4\frac{\partial^4 n}{\partial x^2\partial y^2}+\frac{h^6}{180}\cdot\left[\frac{\partial^6 n}{\partial x^6}+\frac{\partial^6 n}{\partial y^6}\right]\\ &\quad+\frac{h^6}{12}\cdot\left[\frac{\partial^6 n}{\partial x^4\partial y^2}+\frac{\partial^6 n}{\partial x^2\partial y^4}\right]+O(h^8). \end{aligned} \tag{9b}$$

In order to deduce conveniently, the term on the right-hand side in Poisson equation (7) is denoted by f, then, the following equations are derived to achieve the following fourth-order precision:

$$\frac{\partial^4 n}{\partial x^4}=\frac{\partial^2 f}{\partial x^2}-\frac{\partial^4 n}{\partial x^2\partial y^2}, \tag{10a}$$

$$\frac{\partial^4 n}{\partial y^4}=\frac{\partial^2 f}{\partial y^2}-\frac{\partial^4 n}{\partial x^2\partial y^2}. \tag{10b}$$

Summing Eqs. (10a) and (10b) yields

$$\frac{\partial^4 n}{\partial x^4}+\frac{\partial^4 n}{\partial y^4}=\frac{\partial^2 f}{\partial x^2}+\frac{\partial^2 f}{\partial y^2}-2\cdot\frac{\partial^4 n}{\partial x^2\partial y^2}. \tag{10c}$$

Secondly, the idea of undetermined coefficients is used to construct the desired difference scheme with fourth-order precision, which is written as

$$\frac{a\cdot M+b\cdot N+c\cdot n_0}{h^4}=K+O(h^4), \tag{11a}$$

where K is a constant, and the a, b, and c are the undetermined coefficients which need to be determined. Substituting Eqs. (9a), (9b), and (10c) into Eq. (11a), we have

$$\begin{aligned}&\frac{a\cdot M+b\cdot N+c\cdot n_0}{h^4}\\ &=\frac{4a+4b+c}{h^4}\cdot n_0+\frac{(a+2b)}{h^2}\cdot f_0\\ &\quad+\frac{1}{12}(a+2b)\left[\frac{\partial^2 f}{\partial x^2}+\frac{\partial^2 f}{\partial y^2}\right]_0\\ &\quad+\frac{1}{12}(8b-2a)\frac{\partial^4 n}{\partial x^2\partial y^2}+O(h^4).\end{aligned} \tag{11b}$$

Comparing Eq. (11a) with Eq. (11b), the following relationship should be satisfied, that is,

$$4a+4b+c=0,\quad -2a+8b=0. \tag{12}$$

It is easily found that equation (12) has many solutions, and only a simple set is given by

$$a=4,\quad b=1,\quad c=-20. \tag{13}$$

Finally, the final expression for the developed difference scheme with the fourth-order precision is given as

$$\begin{aligned}n_0 &= \frac{n_1+n_2+n_3+n_4}{5}+\frac{n_5+n_6+n_7+n_8}{20}-6h^2 f_0\\ &\quad-\frac{h^4}{2}\left[\frac{\partial^2 f}{\partial x^2}+\frac{\partial^2 f}{\partial y^2}\right]_0.\end{aligned} \tag{14}$$

Note that expression (14) is used to compute the discrete refraction index distribution in a 2D plane by iterative computations. Thus, it is necessary to set an error limit such that the iterative computations are ceased. In this study, the algebraic difference between two neighboring iterative computations is chosen as the judgment condition, and the error limit is set to be 1.0×10^{-8}.

3.3. Density and temperature reconstruction

Because the refractive index distribution in a 2D computational plane can be obtained by solving the Poisson equation with the developed fourth-order difference scheme, then, the density distribution in the plane can be easily calculated by the Gladstone–Dale relation presented in Eq. (3), given as

$$\rho=\frac{n-1}{K_{\mathrm{GD}}}. \tag{15}$$

On the other hand, for the temperature distribution in the plane, it is difficult to solve exactly because the temperature is related to not only density but also pressure by the gas-state equation, given by

$$P=\rho\cdot R_{\mathrm{gas}}\cdot T, \tag{16}$$

where P is the pressure, R_{gas} is the gas constant which is approximately 287 for standard air, and T is the temperature.

However, for the open environment in which the gas movement is absolutely free, the hypothesis that the gas flow in this space is of iso-pressure is reasonable. Consequently, the temperature distribution in the computational plane can be calculated by using this hypothesis, that is,

$$T=\frac{\rho_0\cdot T_0}{\rho}, \tag{17}$$

where ρ_0 and T_0 are the density and temperature of an undisturbed flow field, respectively, and both of them are obtained by being measured before or after experiment.

4. Experimental arrangement and conditions

The experimental arrangement is shown in Fig. 6. It is seen that the BOS system built in this study consists of a background with randomly distributed dots, a CCD camera with high spatial resolution (4000×2660 pixels, that is, the spatial resolution of a recorded image is about 73.8 μm/pixel), and a candle which is used to produce a disturbed flow field. For the cases of light from the background passing through a disturbed and an undisturbed flow field respectively, the images of the background are recorded by the CCD camera with 30 frames per second. The images should be recorded as follows: first, for the undisturbed flow field, the reference images are generated by recording the background pattern before the experiment. Second, for the disturbed flow field which leads to background-element displacements in the imaging plane of the camera, the disturbed images are generated by recording the background pattern during the experiment.

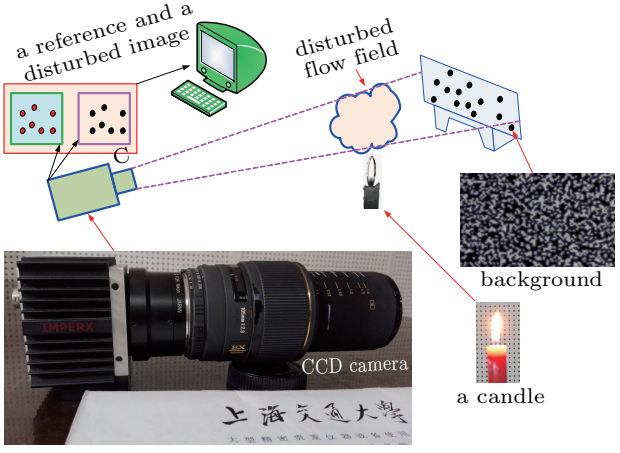


Fig. 6. (color online) Experiment arrangement of the built BOS system.

As shown in Fig. 6, the specific experiment arrangement is as follows: the distance from the background to the center of the disturbed flow field (i.e., Z_D) is 37.5 cm, the distance between the background and the lens (i.e., Z_B) is 95.6 cm, and the distance between the lens and the imaging plane (i.e., Z_I) is 11.9 cm. Note that the central axis of the lens and the centre of the disturbed flow field should be in the same upright plane which is also vertical to the background.

As mentioned above, the procedure for reconstructing the density and temperature field of a flame-induced disturbed flow can be summarized as follows. First, the background-element displacements are calculated via a reference image and a disturbed image by using the cross-correlation algorithm at a sub-pixel-level. Second, the refractive index field is computed by solving the Poisson equation with the developed fourth-order difference scheme. Third, the density and temperature are reconstructed by utilizing Eqs. (15) and (17), respectively.

5. Results and discussion

5.1. Undisturbed flow field

The temperature of the undisturbed flow field, namely the room temperature of our laboratory, is measured before the experiment and is about 300 K. On the other hand, the density of the undisturbed flow is obtained by inquiring the standard atmosphere parameters and it is about 1.161 kg/m^3 in the present study. In order to validate the precision of the built BOS system, the undisturbed flow whose temperature and density have been measured is tested. According to the reconstruction procedure listed above, two reference images recorded at different time instants before experiment are used to reconstruct the density and temperature distribution of a 2D computational plane, such as the central plane of the undisturbed flow field, and the results are shown in Figs. 7, in which the background-element displacements obtained by comparing the two reference images via the cross-correlation algorithm are also presented.

It is seen in Fig. 7 that the sizes of the investigated flow field are 3500×2000 pixels in the horizontal and vertical directions, respectively. The displacements of most of background-elements are approximately less than 0.025 pixel (i.e., about 1.84 μm), which means that the difference between the two reference images is very tiny and it is just consistent with the fact that the two reference images are both recorded from the identically undisturbed flow. In addition, both the temperature and density distribution that are obtained from BOS are also consistent with those from measurements (see Figs. 7(b) and 7(c)). Thus, it indicates that the built BOS system can be used to reconstruct the temperature and density distribution of the undisturbed flow field, and its applicability for reconstructing temperature and density distribution of the disturbed flow field will be investigated in the following subsection.

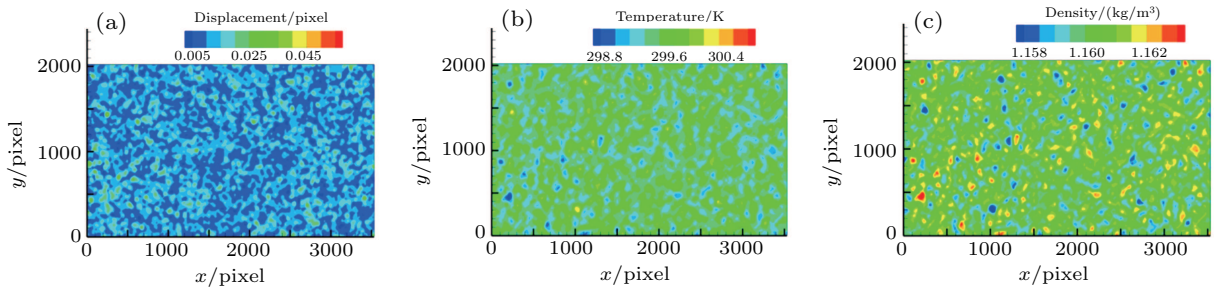


Fig. 7. (color online) The reconstructed temperature and density distribution of the undisturbed flow field, which are obtained by BOS from two reference images ($d = 16$ pixels).

5.2. Disturbed flow field caused by a burning candle

For the case of the disturbed flow field, the central plane of the disturbed flow field which is equivalent to the symmetrical plane of the flame is taken as the computational plane. As shown in Fig. 6, the candle is out of the viewing field of the camera, and the actual distance from the flame tip of the burning candle to the underneath boundary of the background is about 7.5 cm. Figure 8(c) shows the background-element displacements obtained by comparing a reference image (see Fig. 8(a)) with a disturbed image (see Fig. 8(b)), where the yellow vectors also reveal the density gradient of the disturbed flow field.

As shown in Fig. 8(c), the displacements of background-elements nearby the centre line of the flame are much greater than those of the rest of the background, which implies that the fluid over the flame is disturbed more severely than those in the left and right sides of the background, and it is consistent with the physical knowledge. For the present BOS setup, the computed maximum of background-element displacements is about 1.71 pixels, so the employed interrogation window of 32×32 pixels is able to ensure that the elements do not traverse the boundaries of the interrogation window when the cross-correlation computation is performed. According to Ref. [17], the accuracy about 97%–98% can be achieved for background-element displacements more than 1.0 pixel.

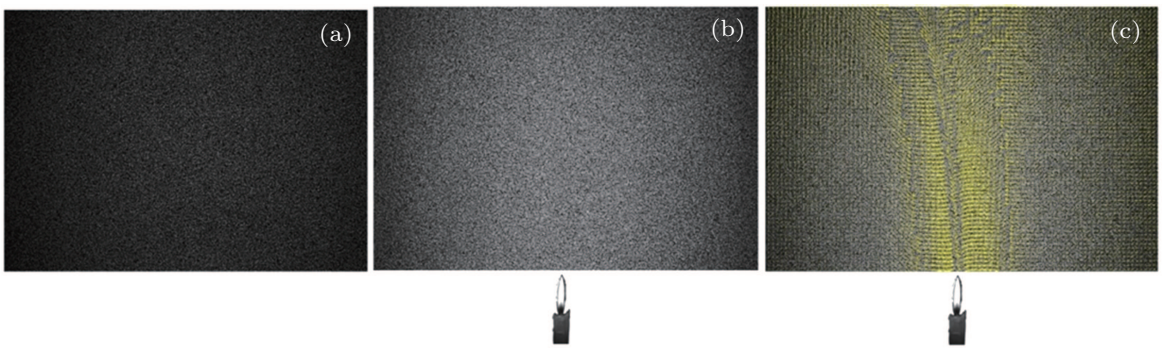


Fig. 8. (color online) Background images: (a) without density gradient; (b) with density gradient due to a flame-induced disturbed flow; (c) difference between image (a) and image (b) that is obtained by the cross-correlation algorithm, where the yellow vectors show the local displacements of the background-elements.

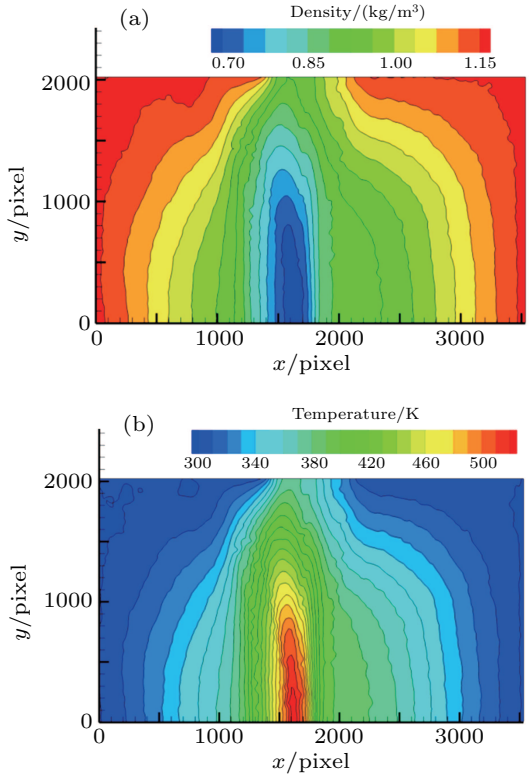


Fig. 9. (color online) Reconstructed (a) density and (b) temperature distribution of disturbed flow field caused by a burning candle ($d = 16$ pixels).

Similarly, the reconstruction procedure listed above is applied to a reference image and a disturbed image to reconstruct the density and temperature distribution of the computational plane, and the reconstructed results are displayed in Fig. 9. It is seen that the density and temperature gradients near the centre line of the flame are especially larger than those of the rest of the computational plane, and these are consistent with the background-element displacements shown in Fig. 8(c). Furthermore, the shapes of both the density and temperature distribution nearby the centre line of the flame are very similar to those of the real flame. Note that the density and temperature distribution of the disturbed flow are reconstructed via a reference image and a disturbed image, rather than a reference image and an averaged image of some disturbed images, so neither the reconstructed density nor the temperature distribution is completely symmetrical with respect to the centre line of the flame. In other words, the reconstructed density and temperature distribution in the current study exactly reflect the dynamic characteristic of the disturbed flow field because a disturbed image is just recorded at one time instant.

Taking the temperature distribution for example, six spots along the centre line are chosen as the measuring points for comparing the reconstructed temperatures along the centre line of the flame with those from manual measurements as shown in Fig. 10, where the right part shows a digital thermometer with a measuring range from −50 °C to 400 °C, and its temperature resolution is 0.1 °C.

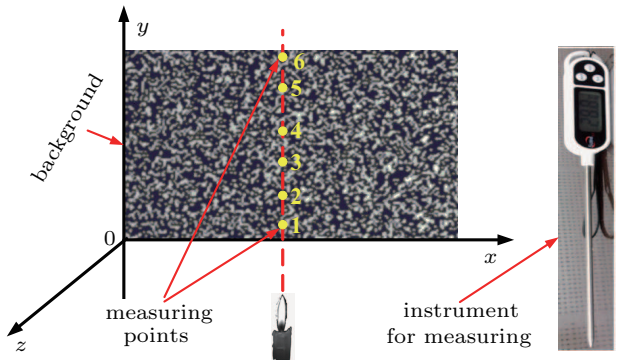


Fig. 10. (color online) Schematic diagram of temperature measurement along the centre line of the flame.

Table 1 presents a temperature comparison between reconstructed results and manual measurements for the six spots. It is observed that the reconstructed temperature of every spot is close to that from measurement, although the algebraic difference for each spot is different. For all the six spots, the maximal difference in temperature between reconstruction and measurement is about 8.4 K, which indicates that the reconstructed results (e.g., temperature distribution) have good accuracy.

Table 1. Comparison of temperature between reconstructed results and measurements for the six spots. Note: The measurement of every measuring spot is actually the average value over some measured temperatures at this measuring spot, and the distances of measuring spots from underneath the boundary of the background are about 141, 718, 1032, 1333, 1600, and 1950 pixels respectively.

Temperature/K	Spot 1	Spot 2	Spot 3	Spot 4	Spot 5	Spot 6
Reconstructed results	526.1	503.7	484.6	447.9	408.7	387.5
Measurements	531.5	510.3	476.2	441.5	416.4	381.3

5.3. Influence of step length on reconstruction accuracy

As displayed in Fig. 11, the step length of the interrogation window, denoted by d, refers to the spacing between two adjoining interrogation windows in the horizontal and vertical direction, and the step length in both directions are set to be the same for simplicity. It is, without a doubt, that the step length has an important influence on the accuracy of the reconstructed density and temperature. From Fig. 11, it is found that the smaller the step length, the more interrogation windows in the search region, which means that the area processed by the cross-correlation algorithm is closer to the whole search region, so more obtained data can be used to reconstruct density and temperature. For this reason, this section discusses the influence of the step length on the reconstruction accuracy.

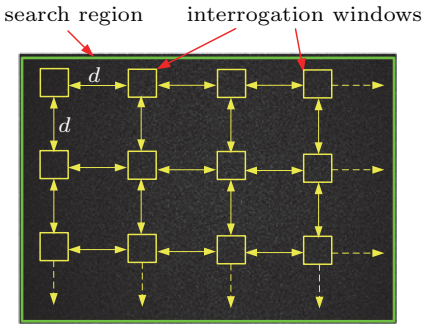


Fig. 11. (color online) Schematic diagram of the interrogation windows arranged in a reference image.

The values of constant d are set, respectively, to be 8, 16, 24, 32, and 48 pixels to explore the influence of step length on the reconstruction accuracy. Given the size of the interrogation window is 32×32 pixels, that is, the step length varies from 0.25 to 1.5 times the interrogation window in both horizontal and vertical directions. For each step length, the density and temperature distribution of the flame-induced disturbed flow field are reconstructed by the built BOS system. In order to compare quantitatively with measurements of temperature, only the temperature distribution along the centre line of the flame is extracted and presented. The comparison between reconstructed results and measurements is shown in Fig. 12, where the presented measurement value of each measuring point is actually the averaged result obtained by averaging over a number of measured data for each measuring point.

From Fig. 12, it is seen that the curve shapes for different step lengths are similar and each curve near the six measurements with various deviations, which implies that all the reconstructed results obtained from different step lengths are able to reveal the real variation tendency of temperature along the center line of the flame but have different accuracies. Specifically, for the cases of $d = 8$, 16, and 24 pixels, the reconstructed results are quite close to the measurements; whereas for the cases of $d = 32$ and 48 pixels, the discrepancies between reconstructed results and measurements are obvious, and the larger the step length, the more serious the deviation is. In addition, the fluctuation of each curve is gradually enhanced with increasing step length. Comparing the step length with the size of the interrogation window (i.e., 32 pixels in both directions), a notable feature is found, that is, for the step length which is less than 32 pixels, such as $d = 8$, 16, and 24 pixels, the reconstructed results have satisfactory precisions, whereas for the step length which is equal to or greater than 32 pixels, such as $d = 32$, and 48 pixels, the accuracy of reconstructed results decreases with increasing step length. Therefore, it can be concluded that the step length should be less than the size of the interrogation window for obtaining a fine reconstruction accuracy.

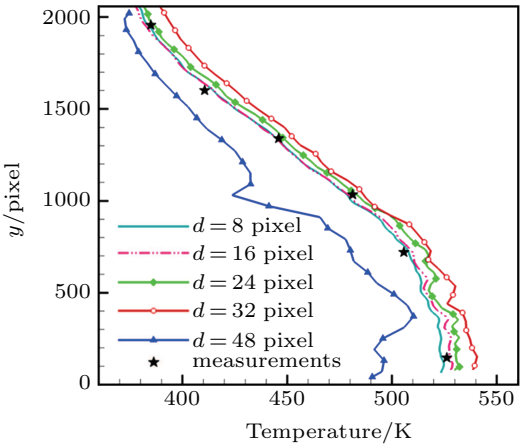


Fig. 12. (color online) Comparisons between measurements and reconstructed results for different steps.

6. Conclusions

In this paper, we study the density and temperature reconstruction of a flame-induced disturbed flow field based on the BOS technique. Both the cross-correlation algorithm with sub-pixel accuracy and the fourth-order difference scheme are used to reconstruct the density and temperature distribution. An experiment is performed to validate the built BOS system, and the results clearly indicate that the density and temperature of the flame-induced disturbed flow field can be reconstructed exactly compared with manual measurements. In addition, the

influence of step length on reconstruction accuracy is also discussed and it is found that the step length should be less than the size of the interrogation window in order to make the reconstructed result have a satisfactory precision.

References

[1] Guo G M, Liu H and Zhang B 2016 *Appl. Opt.* **55** 4741

[2] Gao Q, Yi S H, Jiang Z F, He L and Xie W K 2013 *Chin. Phys. B* **22** 014202

[3] Yin J, Yu L Y, Liu X, Wan H, Lin Z Y and Niu H B 2011 *Chin. Phys. B* **20** 014206

[4] He L, Yi S H, Tian L F, Chen Z and Zhu Y Z 2013 *Chin. Phys. B* **22** 024704

[5] Hinsberg N P and Rosgen T 2014 *Exp. Fluids* **55** 1720

[6] Settles G S 2001 *Schlieren and shadowgraph techniques: visualizating phenomena in transparent media.* (Heidelberg: Springer Press) p. 118

[7] Venkatakrishnan L and Meier G. E 2004 *Exp. Fluids* **37** 237

[8] Meier G E 2002 *Exp. Fluids* **33** 181

[9] Meier G E 1999 *New optical tools for fluid mechanics. In: Proceedings of the* 8*th international symposium on flow visualization*, Sorrento, Italy, p. 226

[10] Dalziel S B, Hughes G O and Sutherland B R 2000 *Exp. Fluids* **28** 322

[11] Richard H and Raffel M 2001 *Meas. Sci. Technol.* **12** 1576

[12] Yamamoto S, Tagawa Y and Kameda M 2015 *Exp. Fluids* **56** 93

[13] Venkatakrishnan L 2005 *AIAA J* **43** 1574

[14] Mizukaki T 2010 *Shock Waves* **20** 531

[15] Sourgen F, Leopold F and Klatt D 2012 *Optics and Lasers in Engineering* **50** 29

[16] Atcheson B, Heidrich W and Ihrke I 2009 *Exp. Fluids* **46** 467

[17] Vinnichenko N A, Uvarov A V and Plaksina Y Y 2012 15*th International Symposium on Flow Visualization*, June 25–28, 2012, Minsk, Belarus, p. 1098

[18] Wang G J, Yang Z J, Meng S, Wang M X and Zhong Y J 2016 *Journal of Experiments in Fluid Mechanics* **30** 103 (in Chinese)

[19] Raffel M 2015 *Exp. Fluids* **56** 60

[20] Debella-Gilo M and Kääb A 2011 *Remote Sensing of Environment* **115** 130

[21] Nobach H and Honkanen M 2005 *Exp. Fluids* **38** 511

[22] Liu Y and Gao F 2010 *Journal of WUT* **32** 873 (in Chinese)